PREPRINT UCRL-78434

CONF-761025-4
CONF-761108--23

Lawrence Livermore Laboratory

Spatially and Temporally Resolved X-Ray Emission From Imploding Laser Fusion Targets

D. T. Attwood, L. W. Coleman, M. J. Boyle, D. W. Phillion,
J. E. Swain, K. R. Manes, and J. T. Larsen

September, 1976

This paper was prepared for presentation at the 10th European Conference on Laser Interaction with Matter, Palaiseau, France, October 18-22, 1976

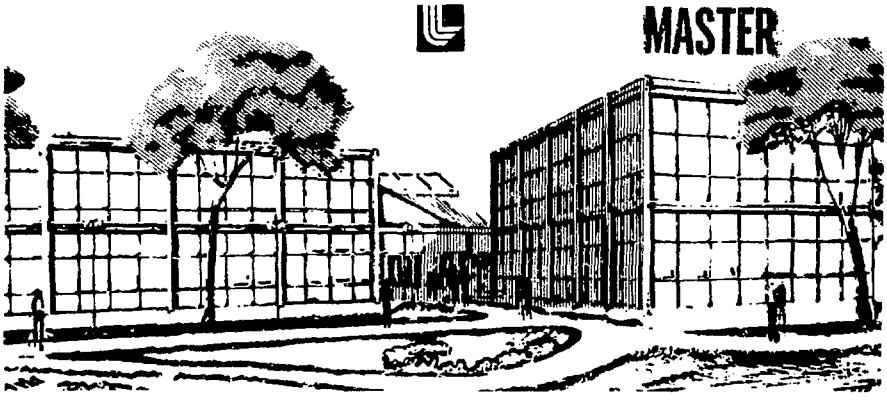

SPATIALLY AND TEMPORALLY RESOLVED X-RAY EMISSION FROM IMPLODING LASER FUSION TARGETS

D. T. Attwood, L. W. Coleman, M. J. Boyle
D. W. Phillion, J. E. Swain, K. R. Manes and J. T. Larsen
Lawrence Livermore Laboratory, University of California
Livermore, California 94550

Abstract

The Livermore 15 psec x-ray streak camera has been used in conjunction with 6 μm diameter pinholes to record well resolved implosion histories of DT filled laser fusion targets. The space-time compression data provide clearly identified implosion velocities, typically 3 x 10^7 cm/sec for two-sided clamshell irradiation of 70 μm, .5 μm wall DT filled glass microshell. Single-sided irradiation results show hydrodynamic convergence at the target center, followed by an asymmetric but two-sided target disassembly. These experiments were performed at the two arm Janus Laser facility, which typically delivered a total of 0.4 TW in a 70 psec pulse for these experiments.

Introduction

Experiments designed to study laser driven implosions of glass microshells are underway in several laboratories around the world. The ultimate goal of these experiments is to drive the encapsulated deuterium-tritium fuel to a sufficiently high density and temperature that the resultant thermonuclear reaction produces a net energy gain[1, 2]. In preliminary experiments it has been shown that modest compressions are achieved[3], and that the resulting neutrons are of a thermonuclear origin[4]. It is important that these early experiments be understood in sufficient detail that future experiments can be accurately designed. Because of the high densities and temperatures involved, x-ray emission from the compressed target provides a primary source of data regarding dynamics of the implosion process. A typical implosion experiment involves an approximately 100 micron initial diameter target which implodes to a fraction of its initial size on a time scale of roughly 100 picoseconds. The x-ray data must therefore be resolved spatially to microns and temporally to several picoseconds in order to provide direct data describing the heating and implosion processes. However, diagnostics available to date have not had the capability of simultaneously providing the required space-time resolutions. Time integrated x-ray imaging studies provide spatially resolved photographs showing target compression[3,5]. Spatially integrated streak camera studies provide temporally resolved x-ray spectral signals interpretable in terms of implosion times[6, 7]. In this paper we report the first temporally resolved x-ray images of laser compressed targets with sufficient resolution to continuously follow the implosion process[8]. The resultant space-time characteristics provide directly observable implosion velocities, and as such provide direct, detailed data of the type required for meaningful comparison with numerical simulations.

Image Formation and Detection

In an earlier paper[7] we discussed use of our 15 picosecond x-ray streak camera to record spectrally and temporally resolved x-ray emission from laser compressed targets. Here we discuss the extension of that work to time resolved pinhole photography[9].

*Work performed under the auspices of the U. S. Energy Research and Development Administration under contract No. W-7405-Eng-48.

A schematic diagram of the general concept appears in Figure 1. An x-ray pinhole is used to image the target, with its own x-ray emission, on the slit of the streak camera. The one dimensional image seen by the slit-shaped cathode is then streaked in time, giving a space-time history of the target implosion. The imaging system must be chosen such that a spatially well resolved, accurately aligned x-ray image illuminates the photocathode. In addition, the image must be of detectable intensity.

As indicated above, x-ray pinholes are used in the work reported here, primarily because they combine ease of construction and large magnification with reasonable spatial resolutions in the micron range when properly designed with respect to geometrical and diffractive effects. For given wavelength λ and object distance p, the optimum pinhole diameter d, for a large magnification camera, is given by [10-16]

$$d \simeq 1.6\sqrt{\lambda p} \qquad (1)$$

For 2 keV x-rays ($\lambda \simeq 6$ Å) and an object distance p of 1 cm, the optimum pinhole diameter is approximately 4 μm. For smaller pinhole diameters obtainable spatial resolution is seriously degraded by diffraction. For larger pinholes, spatial resolution is essentially given by the pinhole diameter. In the work presented here, a 6 μm diameter x-ray pinhole is employed.

It is evident upon inspection of Figure 1 that a vertical displacement of one target radius from the optimum position renders the image tangential to the streak camera slit and therefore unphotographable. Considering that we are interested in 60 - 120 μm diameter targets, and that these implode to a fraction of their initial radius, severe requirements on alignment accuracy are imposed, typically of several microns. The difficulty that this generates resides in the fact that the x-ray pinhole is chosen to be near diffraction limited at 6 Å, and a sufficiently intense

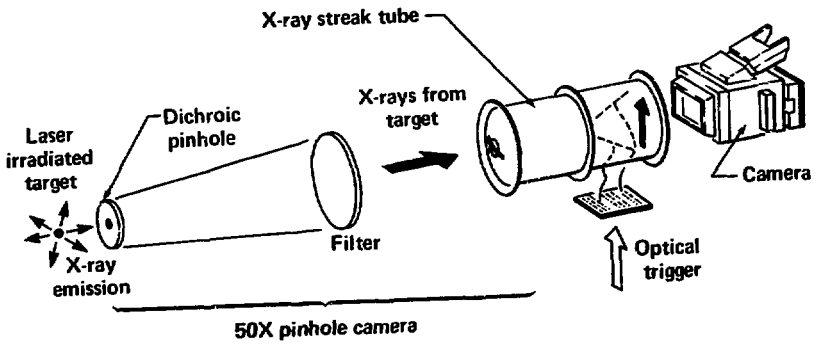

Figure 1. Schematic diagram showing the laser irradiated target, a 50x pinhole camera, and a simplified representation of the x-ray streak camera. Note that a vertical target displacement of one radius from the ideal position renders the image tangential to the slit shaped cathode, and therefore undetectable.

alignment source does not exist at that wavelength. Instead we seek to use a convenient visible alignment technique employing a CW He-Ne laser at 6328 Å. For the given geometry and near optimum x-ray pinhole diameter, this factor of 1000 difference in wavelength causes severe diffraction and essentially renders the visible alignment source useless. A solution to this apparent conflict is to construct composite pinholes[17] which appear small to x-ray wavelengths, but large to visible wavelengths. The use of x-ray absorbing, visibly transparent glass to construct such pinholes is discussed in references 8 and 16.

Pinhole Design and Alignment

As mentioned in the previous section, the crucial feature of these experiments is pinhole-target alignment. With 60 μm diameter targets compressed to a fraction of their initial size, alignment accuracies of several microns are required to keep the x-ray image centered on the slit cathode of the streak camera. With pinhole sizes chosen to be near diffraction limited to 6 Å x-rays, it is evident that composite pinholes[16, 17] are required to permit simple alignment, with a 6328 Å He-Ne laser. Such pinholes appear appropriately small at x-ray wavelengths, but considerably larger and not overly diffracting for the visible alignment source. A typical composite pinhole is shown in Figure 2.

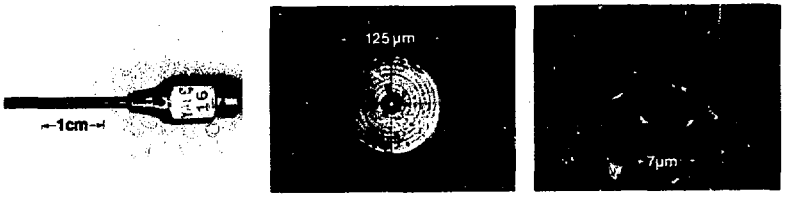

Figure 2. A typical composite pinhole is mounted on the end of a 16 gauge hypodermic needle, as shown in (a). A 125 micron diameter hole is mechanically drilled in a 12 micron thick gold foil, and then covered with a thin (5-10 micron thick) layer of x-ray absorbing, visibly transparent glass. A smaller (3-10 micron) x-ray pinhole is then laser drilled concentrically with the larger hole as shown in (b). A scanning electron microscope picture of the laser drilled hole is shown in (c). Composite pinholes have been formed with both tungsten phosphate and tantalum silicate glasses.

The pinhole is mounted on a hypodermic needle, as seen in Figure 2 (a). A 125 μm diameter hole is mechanically drilled in the gold foil and then the entire gold foil is covered in this case with a 9 μm thick disc of 66% by weight tungsten phospate glass[18]. This glass has an x-ray absorptance of 10^{+5} in the spectral region of interest, and a visible transmittance of 13%. A 7 μm diameter hole is then laser drilled concentrically with the larger 125 μm diameter hole, as shown in Figure 2 (b). A closeup view of

the x-ray pinhole, taken with a scanning electron microscope, is shown in Figure 2 (c). Pinholes in the 3-10 μm diameter range have been constructed in the tungsten phosphate glass and also in 20 μm thick tantalum silicate glass[19].

The visible alignment scheme used in conjunction with composite pinholes is shown in Figure 3. The focal length of the lens is chosen to produce a focal region waist midway between pinhole and target. By appropriate clipping of the beam at the focusing lens, a set of Airy rings[20] modulate the waist pattern. The second dark ring is set approximately at 125 μm to allow accurate alignment of the large (125 μm) hole of the composite pinhole. The x-ray pinhole is now centered in the optical alignment pattern, within a concentricity error of 2 or 3 microns for the composite pinholes. The transmitted interference pattern, now somewhat affected by pinhole diffraction, propogates on to the target plane one centimeter away. The target is then moved to a central position as shown in the successive photographs of Figure 4. With the cathode slit, pinhole, and target in alignment, the system is ready for target irradiation and compression experiments.

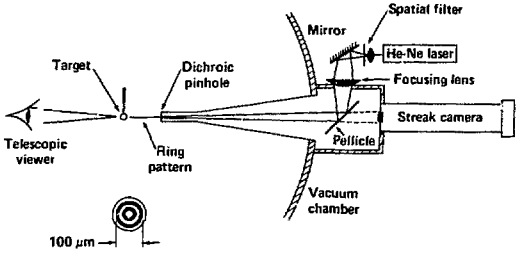

Figure 3. Target alignment scheme employing a He-Ne laser, a focusing lens, and a set of Airy rings. Both the composite pinhole and the target are centered in the visible diffraction pattern.

Figure 4. Three steps to easy target alignment via use of the Airy diffraction pattern described in Figure 3. The successive photographs show the target being moved to a central position where it will be properly aligned with both the pinhole and x-ray streak camera cathode.

Space-Time Implosion Diagrams

Results obtained during recent implosion experiments with Livermore's JANUS laser facility[21-23] are presented in Figures 5-7 for three nearly identical targets. These experiments involved the irradiation and compression of typically 68 micron diameter, 0.5 micron thick DT filled glass microshells. Using ellipsoidal focusing mirrors (NA=0.99), the laser delivered approximately 0.45 TW in a typical 70 psec, two-sided irradiation experiment. X-ray imaging and filtering were obtained with a 6 micron diameter tantalum pinhole and a 125 micron thick beryllium filter, respectively.

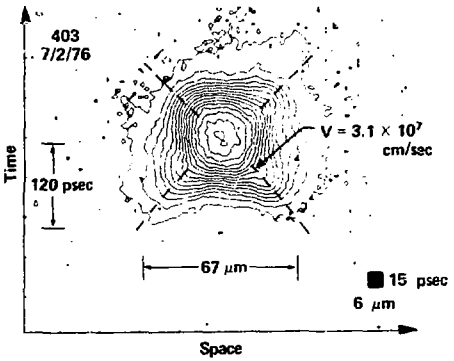

Fig. 5. Isodensity contours obtained from x-ray pinhole/streak record. The target had a wall thickness of 0.51 microns, a DT fill of 1.32 mg/cc, and upon irradiation produced 1 x 10^6 neutrons. Two sided target irradiation consisted of 17.2 J and 16.4 J, 75 psec FWHM pulses.

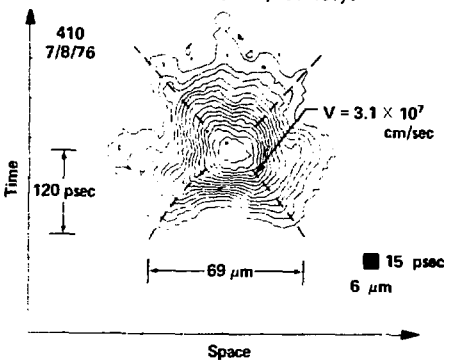

Fig. 6. Isodensity contours obtained directly from x-ray pinhole/streak record. The target had a wall thickness of 0.44 microns, a DT fill of 1.67 mg/cc, and upon irradiation produced 1 x 10^6 neutrons. Two sided target irradiation consisted of 14.6 J and 15.6 J, 64 psec FWHM pulses.

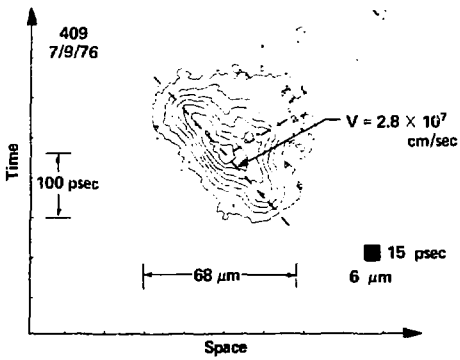

Fig. 7. Isodensity contours obtained directly from x-ray pinhole/streak record. The target had a wall thickness of 0.57 microns, a DT fill of 1.82 mg/cc, and upon irradiation produced 2 x 10^5 neutrons. Single sided target irradiation consisted of a 16.9 J pulse of approximately 70 psec FWHM.

The space-time implosion diagrams presented in Figures 5-7 show isodensity film contours obtained directly from the respective pinhole/streak camera records. Shaded blocks in the lower right hand corner of each diagram display the approximate space-time resolutions of 6 microns and 15 picoseconds.

The results presented in Figures 5 and 6 show two rather similiar implosions, except that one is somewhat more symmetric (Figure 5), while the other shows more pronounced details of target acceleration. Both produced final implosion velocities of approximately 3.1 x 10^7 cm/sec, as seen in the illustrations. Further details from these two-sided irradiation experiments are presented in the following paragraph. In the third experiment, described by Figure 7, target irradiation was purposely blocked on one side so as to observe details of a single sided implosion experiment. This one sided irradiation experiment is very interesting in that it shows hydrodynamic convergence at the target center, and an asymmetric but two sided disassembly as the compressed core coasts for some distance.

Taking target 410, Figure 6, as representative of these implosion experiments we describe it further in Figures 8 and 9. The data has been converted here to x-ray exposure vs. space and time by removing the D vs. log E properties of the recording film. Taking cuts of the modified data in Figure 6 at discrete times and spatial positions we obtain the profiles presented in Figures 8 and 9. Figure 8 shows spatial contours of x-ray emission at several discrete times. At an early time the spatial profile shows two distinct emission regions corresponding to the oppositely directed

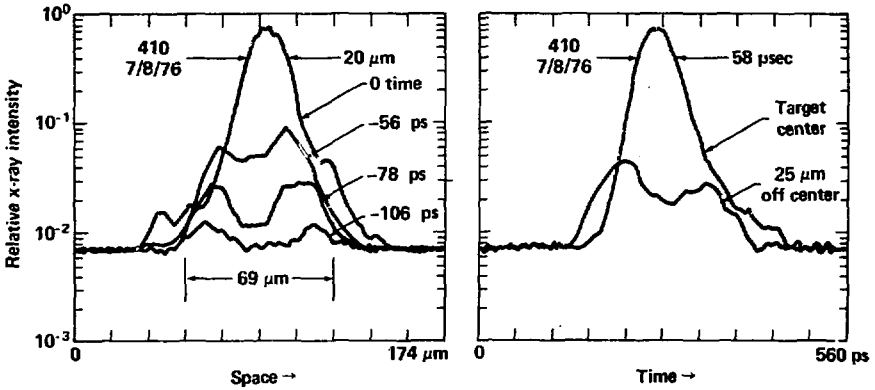

Figure 8. Spatial profiles showing the implosion of 410 at various times. Emission from opposite sides of the imploding shell are observed to coalesce and finally form an intense stagnation region near the target center.

Figure 9. Temporal profiles of x-ray emission from the target center and from a position 20 microns to one side. The latter shows a double humped behavior as intense x-ray emission passes this radial position once during implosion and once during post-compression disassembly.

sides of the imploding shell. At a later time, but before peak compression, the two regions grow significantly in intensity and begin to coalesce. At a still later time the two regions have merged into a single, stagnated core of peak x-ray intensity. Final target disassembly in the post-compression period is omitted for clarity. Figure 9 shows x-ray temporal profiles for the target center, and for a position 20 microns off center. Note that the latter position displays a two humped behavior as peak radiation passes that radial position once during implosion and once during disassembly. Note that a properly weighted sum of the two temporal profiles in Figure 9 could be used effectively to reconstruct the unimaged profiles presented in Reference 7.

The results presented in the previous paragraph describe the implosion of targets for which the absorbed laser power per unit target mass is relatively high, i.e. greater than 4 GW/ng absorbed, or greater than 0.3 J/ng for a 75 ps FWHM pulse. As observed in Figures 5-9, x-ray emission from these targets monatonically increases during the implosion. Concomitantly, two-dimensional time integrated x-ray microscope images do not display a separated emission ring near the original target wall position. Rather, the microscope images show a continuously increasing emission towards the target center.

A second class of results (the transition is not abrupt) is characterized by smaller absorbed power (or energy) per unit target mass. Time integrated images for this case display a definite ring surrounding a separate, intense core of emission at the target center.[3, 5] A typical space-time implosion, resolved by the techniques described herein, is presented in Figure 10. With an initial diameter of 125 μm, and a wall thickness of 0.86 μm, this target was approximately six times more massive than those described in Figures 5-7. As a result, x-ray emission was decreased for the same laser power, resulting in the weaker recorded image. More significantly, the space-time diagram of Figure 10 shows a significantly different pattern -- islands of x-ray emission at the initial diameter during laser heating, a decline of emission as the target expands inwardly and outwardly ("explodes") and finally the reappearance of significant emission, now from the target center and at a later time. This behavior has been repeated in several experiments, including a lighter target where the laser power was halved. A summarizing array of observed x-ray emissions is shown in Figure 11. Three types of observed data are presented: two-dimensional spatial emission, time resolved spectral signatures, and space-time implosion diagrams. The two basic classes of experiment are evident; those having high and low absorbed power per unit mass.

Summary

Experimental observations of the space-time implosion history of laser compressed targets are presented. Directly observable implosion velocities of 3×10^7 cm/sec are evident for both one and two-sided implosions. Shell acceleration is observed in some experiments. Space-time resolutions for these measurements are approximately 6 μm and 15 psec.

Acknowledgments

C. M. Dittmore and H. F. Finn provided valuable assistance in the reduction and analysis of data. R. F. Wuerker, B. W. Weinstein, G. E. Sommargren, J. W. Houghton, B. Holloway, S. Nakano, E. R. Prochnow, J. Shelby and D. Blackburn have played significant roles in constructing the x-ray pinhole camera. Targets for these experiments were provided under the direction of C. D. Hendricks. Target irradiation experiments were conducted under the direction of H. G. Ahlstrom.

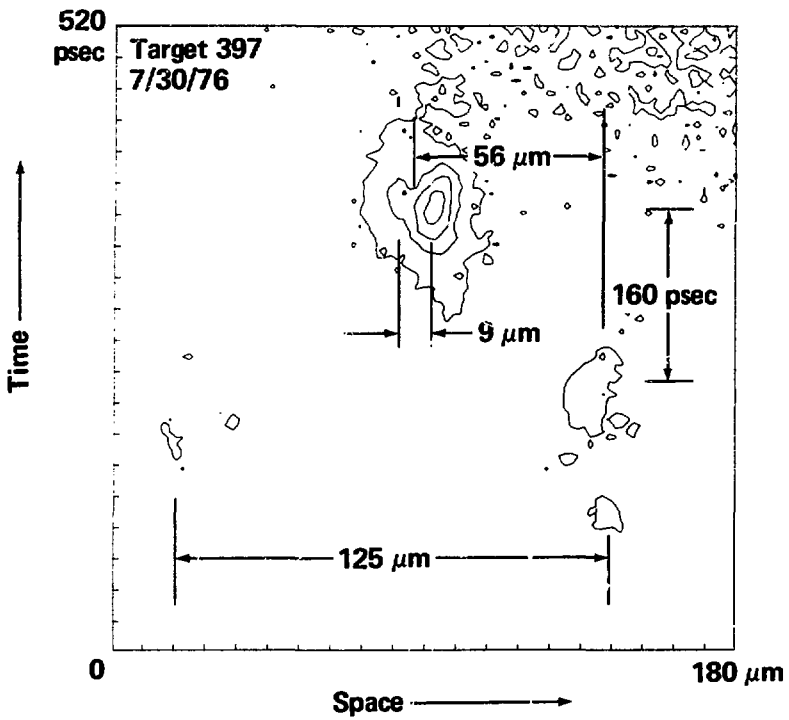

Figure 10. Density contours from space-time resolved implosion of a 125 μm diameter, 0.86 μm thick wall, 0.99 mg/cc DT filled target. Laser irradiation was two sided with a total of 35.5 J in a 79 psec FWHM pulse. Note that late time emission shows a spatially divided core, as was also observed in the time integrated x-ray microscope image for this same experiment (see lower left image in Figure 11).

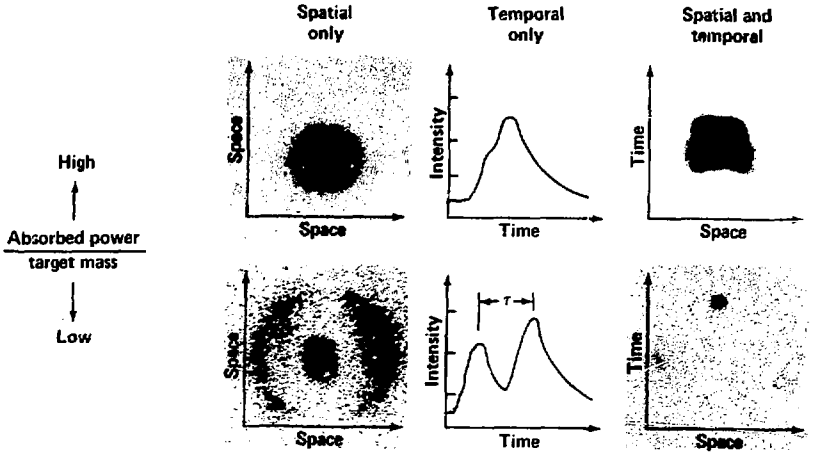

Figure 11. Observed x-ray data for target experiments with high and low absorbed laser power per unit target mass. The three data sets are (from left to right): Two-dimensional (time integrated) x-ray microscope image, time-resolved x-ray spectral studies, and space-time resolved x-ray implosion records.

References

1. J. Nuckolls, L. Wood, A. Thiessen and G. Zimmerman, Nature 239, 139 (1972).
2. J. L. Emmett, J. Nuckolls, L. Wood, Sci. Amer. 230, 24 (1974).
3. P. M. Campbell, G. Charatis, and G. R. Monty, Phys. Rev. Lett. 34, 74 (1975).
4. V. W. Slivinsky, H. G. Ahlstrom, K. G. Tirsell, J. T. Larsen, S. Glaros, G. Zimmerman and H. Shay, Phys. Rev. Lett. 35, 1083 (1975).
5. F. Seward, J. Dent, M. Boyle, L. Koppel, T. Harper, P. Stoering and A. Toor, Rev. Sci. Inst. 47, 464 (1976).
6. D. T. Attwood and L. W. Coleman, XII Intl. Conf. on High Speed Photography, paper DA-1, Toronto, Canada 1976; Bull. Amer. Phys. Soc. 20, 1267 (1975).
7. D. T. Attwood, L. W. Coleman, J. T. Larsen and E. K. Storm, Phys. Rev. Lett. 37, 499 (1976).
8. D. T. Attwood, XII Int'l. Conf. on High Speed Photography, paper DA-2, Toronto, Canada, 1976.
9. In several respects use of an x-ray microscope is preferable for these studies. For instance, large numerical aperture and high spatial resolution are achievable with large object distances. The latter is important both for convenience and resistance to damage from unabsorbed laser light, reaction products, and general target debris. However, as reported in Reference 6, the x-ray streak camera has a spatial resolution of 130 μm at the cathode, necessitating use of a 50x imaging system to obtain reasonable spatial resolution in the target plane. Large magnification x-ray microscopes are presently being constructed at Livermore under the direction of M. Boyle and H. Ahlstrom.
10. B. M. Rovinsky and V. G. Lutsau, appearing in X-Ray Microscopy and Microradiography, edited by V. Coslett et. al. (Academic, New York. 1957), p. 131. These authors obtained 1 micron spatial resolution in well designed x-ray pinhole experiments.
11. R. P. Godwin, appearing in Advances in X-Ray Analysis, edited by R. Gould (Kendall/Hunt, Dubuque, Iowa, 1975), p. 560.
12. G. Reynolds and J. Ward, J. Soc. Phot. Instr. Eng. 5, 3 (1966).
13. R. Swing and D. Rooney, J. Opt. Soc. Amer. 58, 629 (1968).
14. J. Mack and M. Martin, The Photographic Process (McGraw-Hill, New York, 1939), p. 37.
15. S. Tolansky, Curiosities of Light Rays and Light Waves (American Elsevier, New York, 1965), p. 12.
16. D. T. Attwood, B. W. Weinstein and R. F. Wuerker, in preparation.
17. D. T. Attwood, USAEC Patent Disclosure IL-5984 (May 12, 1975).
18. J. J. Rottermel, K. H. Sun, and A. Silverman, J. Am. Ceram. Soc. 32, 153 (1949).
19. The composition of this glass is 60% Ta_2O_5, 20% Ba O, 13% $Si O_2$, and 7% $B_2 O_3$ by weight.
20. M. Born and E. Wolf, Principles of Optics (Pergamon New York, 1975), p. 395.
21. J. F. Holzrichter and D. R. Speck, J. Appl. Phys 47, 2459 (1976).
22. H. G. Ahlstrom and J. F. Holzrichter, Laser Focus 11, 39 (1975).
23. J. F. Holzrichter, H. G. Ahlstrom, D. R. Speck, E. Storm, J. E. Swain, L. W. Coleman, C. D. Hendricks, H. N. Kornblum, F. D. Seward, V. W. Slivinsky, Y. L. Pan, G. B. Zimmerman, and J. H. Nuckolls, Plasma Phys. 18, 675 (1976).